Population Encoding of Spatial Frequency, Orientation, and Color in Macaque V1

JONATHAN D. VICTOR, KEITH PURPURA, EPHRAIM KATZ, AND BUQING MAO
Department of Neurology and Neuroscience, Cornell University Medical College; and Laboratory of Biophysics, The Rockefeller University, New York, New York 10021

SUMMARY AND CONCLUSIONS

1. We recorded local field potentials in the parafoveal representation in the primary visual cortex of anesthetized and paralyzed macaque monkeys with a multicontact electrode that provided for sampling of neural activity at 16 sites along a vertical penetration. Differential recordings at adjacent contacts were transformed into an estimate of current source density (CSD), to provide a measure of local neural activity.

2. We used m-sequence stimuli to map the region of visual space that provided input to the recording site. The local field potential recorded in macaque V1 has a population receptive field (PRF) size of ~ 2 deg^2.

3. We assessed spatial tuning by the responses to two-dimensional Gaussian noise, spatially filtered to retain power only within one octave. Responses to achromatic band-limited noise stimuli revealed a prominent band-pass spatial tuning in the upper layers, but a more low-pass spatial tuning in lower layers.

4. We assessed orientation tuning by the responses to band-limited noise whose spectrum was further restricted to lie within $45°$ wedges. The local field potential showed evidence of orientation tuning at most sites. Orientation tuning in upper and lower layers was manifest by systematic variations not only in response size but also in response dynamics.

5. We assessed chromatic tuning by the responses to isotropic band-limited noise modulated in a variety of directions in tristimulus space. Some lower-layer locations showed a nulling of response under near-isoluminant conditions. However, response dynamics in upper and lower layers depended not only on luminance contrast, but also on chromatic inputs.

6. Responses to near-isoluminant stimuli and to low-contrast luminance modulation were shifted to lower spatial frequencies.

7. We determined the extent to which various temporal frequencies in the response conveyed information concerning spatial frequency, orientation, and color under the steady-state conditions used in these studies. In each case, information is distributed in the response dynamics across a broad temporal frequency range, beginning at 4 Hz (the lowest frequency used). For spatial frequency the information rate remains significant up to at least 25 Hz. For orientation tuning and chromatic tuning, the information rate is lower overall and remains significant up to 13 Hz. In contrast, for texture discrimination, information is shifted to lower temporal frequencies.

INTRODUCTION

The primary visual cortex is perhaps the most extensively studied region of the primate CNS. Single-unit and anatomic studies of the macaque primary visual cortex have revealed an array of interrelated organizational features: for example, variation of ocular dominance and orientation tuning in a modular, anatomically patterned fashion (Hu-

bel and Wiesel 1977). There is evidence that specialization for chromatic sensitivity is correlated with the cytochrome oxidase blobs (Livingstone and Hubel 1984; Tootell et al. 1988), although this is controversial (Leventhal et al. 1993; O'Keefe et al. 1993). The goal of these studies is to characterize the physiological properties of populations of neurons in primary visual cortex of the macaque monkey, and to compare this characterization with the picture currently afforded by single-unit studies.

The standard approach to the analysis of response properties of single neurons relies on stimuli such as bars and gratings, as well as on precise location of the stimulus in the receptive field of the neuron under study. However, in the natural environment, cortical neurons are not usually presented with their optimal stimuli. Furthermore, a near-optimal stimulus for one neuron may simultaneously be a suppressive stimulus or an irrelevant one for its neighbor (for example, because of differences in sensitivity to orientation or spatial phase). The net result of this activity is difficult to predict from current knowledge of single-unit properties.

The present approach does not seek to determine the tuning of individual neurons through the use of stimuli to which they are optimally sensitive, but rather, to examine the visual responses of neural populations. We examined the responses of neural populations through recording of the local field potential elicited by a variety of visual stimuli. We chose to use stimulus sets that consisted of multiple examples of spatial noise, in which the phases of the underlying components were randomized across trials. With this stimulus set, sensitivity to a particular spatial frequency could be determined by averaging responses to isotropic spatial noise centered at the spatial frequency of interest. Similarly, orientation tuning could be determined by examining responses to noise stimuli whose Fourier components had a constrained orientation but random spatial phases, and chromatic tuning could be determined by varying the chromatic modulation of the stimuli.

In broad terms, our results are in agreement with established features of the functional organization of V1, including ocular dominance, spatial tuning, and orientation tuning. A striking overall theme in our results is that spatial tuning, orientation tuning, and chromatic tuning are carried in the dynamics of the population responses, and not its overall size. Temporal coding is known to exist at subcortical levels, primary visual cortex, and extrastriate areas at the level of the single neuron (McClurkin et al. 1991a,b; Richmond et al. 1987). Our results add to these

findings in several important ways. We show that temporal encoding is present at the level of the neuronal population, that it occurs under steady-state conditions, and that its temporal characteristics depend on the modality that is encoded.

A portion of this work was presented at the 1992 meeting of the Society for Neuroscience, Anaheim (Katz et al. 1992).

METHODS

General physiological preparation

Seven adult male cynomolgus monkeys (*Macaca fascicularis*) were studied. The animal was premedicated with atropine 0.04 mg im, and then anesthesia was induced with ketamine 15 mg/kg im potentiated by xylazine 2 mg/kg im (Rompun, Haver). Pupils were dilated with 1% atropine. Flurbiprofen (2.5%; Ocufen, Allergan) was instilled as prophylaxis against ocular inflammation, and the eyelids were temporarily closed to protect the physiological optics. Via cutdowns, catheters were inserted in both femoral veins and one femoral artery. The trachea was cannulated via a midline incision. All incisions were prepped with betadine and infiltrated with 1% xylocaine. In one preparation, supplemental anesthesia during this initial surgery was required and was obtained with thiamylal boluses (1–2 mg/kg iv). Once hemodynamic monitoring, venous access, and tracheal access were established, an infusion of sufentanil (1–6 μg·kg^{-1}·h^{-1} iv; Sufenta, Janssen) was begun and adjusted to maintain anesthesia. One animal failed to respond to sufentanil at 6 μg·kg^{-1}·h^{-1}; in this animal, urethan (400 mg/kg iv loading, 200 mg/kg iv every 12 h) was substituted for sufentanil (Purpura et al. 1990). Dexamethasone (1 mg/kg iv) was administered at the start of the experiment and daily thereafter to reduce cerebral edema. Procaine penicillin G (25,000 U/kg im) and benzathine penicillin G (25,000 U/kg im; Pen BP-48, Pfizer) was administered as prophylaxis against surgical infection.

The animal was then transferred to a stereotaxic frame. Eyelids were retracted with 6–0 chromic gut sutures, and corneas were protected with contact lenses. The dura overlying V1 was exposed via a craniotomy. Before physiological recording but after all surgical procedures and placement in the stereotaxic, paralysis was induced with gallamine triethiodide (7 mg/kg iv bolus, 5–15 mg·kg^{-1}·h^{-1} iv; Flaxedil, Davis and Geck) or pancuronium bromide (0.3 mg/kg iv bolus, 0.3 mg·kg^{-1}·h^{-1} iv). Anesthesia during paralysis was maintained by adjustment of the sufentanil infusion rate and monitored by blood pressure, pulse rate, electrocardiogram (EKG), and electroencephalogram (EEG) patterns. Temperature, monitored with a rectal thermistor, was maintained at 38°C with a thermostatically controlled heating blanket. Ventilator settings were adjusted to maintain an end-expiratory CO_2 at 30–35 mmHg. Supplemental oxygen was administered every 6 h. Hydration (lactated Ringer solution with 5% glucose, 2–3 ml·kg^{-1}·h^{-1}) was maintained throughout the experiment. Gentamicin (5 mg/kg im daily) was added on the 2nd or 3rd day if fever, hypoxia (monitored via a Hewlett-Packard 78354A pulse oximeter placed on the tongue), increased tracheal secretions, or chest auscultation suggested the development of infection. Every 12–24 h, the corneas were irrigated with Ringer, and flurbiprofen was instilled. Local antibiotic (bacitracin, neomycin, and polymyxin B ointment) was applied if a conjunctival discharge was present. Animals maintained in this fashion generally remained in good physiological condition and retained excellent optics for 72 h. Adequacy of the anesthetic protocol was assured by discontinuation of paralysis in one monkey and demonstration of lack of response to noxious stimuli.

Visual stimulation

The positions of the optic disk and foveal pit were mapped onto a tangent screen with a modified hand-held fundus camera. Refraction was optimized for the viewing distance of 114 cm with trial lenses as determined by retinoscopy, and artificial pupils (3 mm diam) were centered in front of the natural pupils. We used two approaches to corroborate the retinoscopic refraction. In one animal we obtained an independent refraction from optimizing the responses of isolated single units (recorded with an Ainsworth electrode). In several animals we measured responses to high spatial frequencies (see below) over a range of refractions that bracketed the retinoscopic refraction. In both cases the optimal response was obtained within 0.5 D of the refraction chosen by retinoscopy.

Visual stimuli were generated on a Conrac 7351 RGB monitor modified for a frame rate of 135 Hz. Mean luminance of the display was 97 cd/m^2. The display was viewed through a circular aperture, to generate a stimulus of diameter 11.5° at a viewing distance of 114 cm. R, G, B. Synchronization signals for the display were generated by specialized hardware [modified from the stimulator of Milkman et al. (1980)] interfaced to a DEC 11/93 computer. Each pixel in the 256 × 256–pixel raster was assigned to 1 of 16 spatiotemporal functions on the basis of values stored in 4 bit planes. Each bit plane of this on-board memory was chosen on a frame-by-frame basis from a preloaded repertoire of 16 alternatives, which enabled rapid interchange among up to 65,536 (=16^4) possible assignments. The intensity versus voltage nonlinearities of the cathode ray tube (CRT) were corrected by independent 12-bit look-up tables for each gun, whose values were determined by photometric measurements of the gun outputs. The emission spectra of the R, G, and B phosphors were determined by a Pritchard PR703 spectrophotometer. This information was used to determine color space coordinates (Derrington et al. 1984) and estimates of cone excitations based on the human photopigments (Smith and Pokorny 1975). Cone-excitation calculations based on similar measurements and apparatus had previously been validated through the use of known protanopes and deuteranopes (Purpura and Victor 1990).

The frame rate of the stimulator provided the synchronization signals for generation of the visual stimuli, as well as for data acquisition by the DEC 11/93. Data were collected at the onset of each frame and exactly halfway through each frame, for a sampling rate of 270.329 Hz (3.7-ms bins). Two kinds of visual stimuli were used: stimuli consisting of abrupt interchange among visual patterns at regular intervals ("periodic stimuli") and m-sequence (Sutter 1987) stimuli. The m-sequence stimuli were used for mapping purposes; the periodic stimuli were used for characterization of response properties.

The periodic stimuli consisted of two types: checkerboard and filtered Gaussian noise. *1*) Checkerboard stimuli were as follows: check sizes ranged from 32 × 32 pixels to 2 × 2 pixels [at the standard viewing distance: 1.43–0.089°; spatial frequencies (along the diagonal) of 0.49–7.87 cycles/deg]. Contrast for checkerboards [$(I_{max} - I_{min})/(I_{max} + I_{min})$] was 1.0. Checkerboards were modulated in time at 2.112 Hz either by contrast reversal (64 frames per cycle, 32 frames per reversal, reversal rate of 4.224 Hz) or pattern appearance (32 frames on, 32 frames off). *2*) Filtered Gaussian noise (FGN) stimuli were stimuli that consisted of presentations of multiple examples of samples of two-dimensional Gaussian noise at a rate of 4.224 Hz (32 frames per example). We describe responses to two kinds of noise: isotropic band-limited noise (Fig. 1*A*), and oriented band-limited noise (Fig. 1*B*). These noise stimuli were constructed from a broadband noise stimulus that contained all frequencies from 1 cycle/screen (0.087 cycle/deg) to 128 cycles/screen (11.1 cycles/deg), with a spectral density proportional to $1/k^2$ at the spatial frequency k. (This pink-
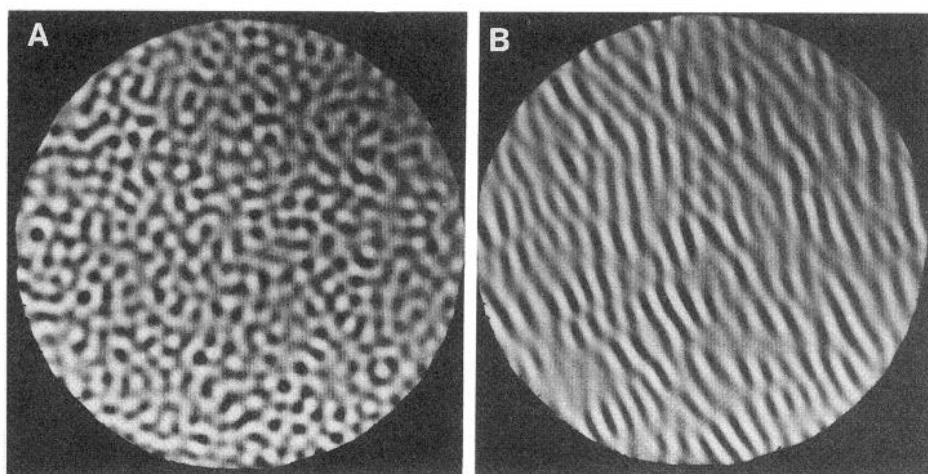
FIG. 1. Examples of filtered Gaussian noise stimuli. *A*: isotropic band-limited noise. *B*: oriented band-limited noise.

noise spectrum was chosen so that there would be a constant amount of power per octave.) The isotropic band-limited noise was generated by restriction of the $1/k^2$ spectrum of the broadband isotropic noise to octaves, ranging from a 2- to 4-cycle/screen stimulus (center frequency 0.245 cycle/deg) to a 64- to 128-cycle/screen stimulus (center frequency 7.87 cycles/deg). The overall contrast of these stimuli were normalized to a standard deviation of 0.4. The oriented band-limited noise stimuli were constructed by further restriction of the spectrum of the band-limited noise to lie within a 45° wedge, and renormalization of the overall contrast to a standard deviation of 0.4.

M-sequence stimuli are complex spatiotemporal patterns in which each region of a multiregion display is modulated by a pseudorandom binary sequence (Sutter 1987). The binary sequence is generated by a linear recursion relationship whose properties guarantee that it is nearly orthogonal to shifts of itself. This property makes m-sequence stimuli particularly efficient for mapping the input to a neural response, because components driven by each region can be extracted by cross-correlation with the input sequence.

We based our m-sequence stimuli on an array of 249 regions covering a nearly circular area (see, for example, Fig. 2). This array was constructed from a 15 × 15 array by deletion of the 4 corner regions and addition of 7 oblong regions adjacent to the middle of each side of the array. Unless otherwise noted, the 221 central regions were 43-min squares; the 28 peripheral regions were 43 × 21 min. Our binary sequence was generated by the order-12 recursion relation $s_n + 12 \equiv s_n + s_{n+3} + s_{n+4} + s_{n+7}$ (mod 2). This sequence of binary values repeats after 4,095 ($2^{12} - 1$) elements. An important consequence of the maximal length of the repeat (see, for example, Sutter 1987) is that distinct temporal shifts of the sequence $s_0, s_1, s_2, \cdots$ are nearly orthogonal. Each region r was assigned a temporal shift ("tap") $D(r)$, and the shifted sequence $s_{0+D(r)}, s_{1+D(r)}, s_{2+D(r)}, \cdots$ was used to modulate region r of the display. The temporal shifts $D(r)$ assigned to each region were separated by a minimum of 16 m-sequence elements. In standard runs we used the convention that $s_n \equiv 0$ (mod 2) corresponded to a contrast $[(I - I_{\text{mean}})/(I_{\text{mean}})]$ of -1 and $s_n \equiv 1$ (mod 2) corresponded to a contrast of $+1$. In inverted-repeat runs (Sutter 1987) we used the opposite convention: $s_n \equiv 0$ (mod 2) corresponded to a contrast of $+1$ and $s_n \equiv 1$ (mod 2) corresponded to a contrast of -1. The frame corresponding to each m-sequence element was presented for four data-collection bins (14.8 ms). Thus taps for each region were separated by a minimum of 236.7 (16 × 14.8) ms, and the repeat period of the stimulus was 60,592.8 (4,095 × 14.8) ms. The autocorrelation property of m-sequences imply that the (temporal) spectrum of the signal presented to each stimulus region is flat up to frequencies that approach the Nyquist frequency ($\frac{1}{2}$ of the sampling rate; here, 33.8 Hz).

Electrophysiological recording

Multicontact electrodes, provided by Dr. Charles Schroeder (Albert Einstein College of Medicine), were used for these studies (Schroeder et al. 1991). In six of the seven animals, we used an electrode built out of a 29-gauge needle (330 µm diam) consisting of 16 stainless steel contacts embedded in epoxy. The 15 proximal contacts were spaced at 150-µm vertical intervals, and the distal contact was 1,000 µm below its nearest neighbor. In the seventh animal, an electrode of similar design but with only eight contacts was used. Contact resistances in saline ranged from 40 to 100 kΩ. The electrode was inserted through a durotomy made under an operating microscope at a location 3–5 mm posterior to the lunate sulcus, at an orientation judged to be perpendicular to the cortical surface, and positioned to avoid superficial cortical vessels. On histological section, recovered tracks were typically within 10° of normal and were always within 30° of normal.

The signals from each contact, referenced to a screw in the frontal bone, were led to a unity-gain field effect transistor (FET) preamplifier. Signals from adjacent contacts were then amplified 10,000-fold by a bank of matched differential amplifiers, filtered (1.0–100 Hz), and led to the DEC 11/93 computer that controlled the experiment. This provided amplified signals that represented bipolar recordings between adjacent electrode contacts. The computer digitized these signals at twice the frame rate, performed preliminary on-line analysis, and stored the data for further off-line analysis.

Data collection and analysis

For checkerboard and FGN stimuli, responses were collected in segments of 15 s, after an initial period of 1.89 s (8 transitions of the checkerboard or FGN stimuli) in which the stimulus was presented but data were not collected. Each stimulus condition was presented four to eight times (usually 6 times) in randomly interleaved runs.

Data analysis common to all periodic stimulus presentations (checkerboard and FGN stimuli) consisted of calculation of the first eight Fourier components of the averaged responses on each of the recorded channels. The uncertainty of these averaged responses was assessed by the T_{circ} statistic (Victor and Mast 1991) applied to Fourier components calculated from each (individual) segment.

For m-sequence stimuli, responses were collected in segments of 60.59 s (1 repeat), after an initial period of 1.89 s of m-sequence stimulation without data collection. Standard and inverse-repeat (Sutter 1987) runs were alternated, with each run presented two to four times. Storage restrictions limited data collection to one or two electrode channels. The first-order m-sequence kernel associated with each region was determined by cross-correlation of the
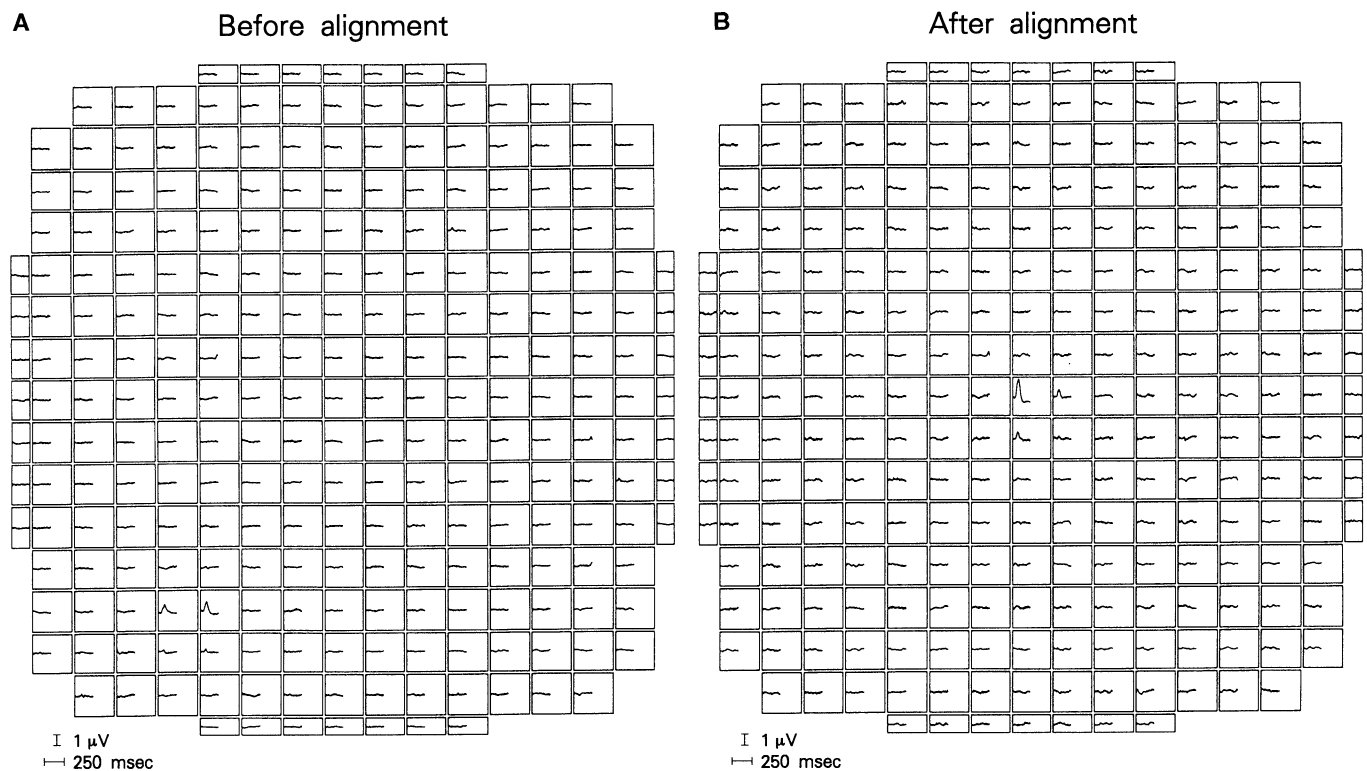
A   Before alignment

B   After alignment

FIG. 2. Example of an alignment procedure based on m-sequence stimulation. Responses to the grid of 249 checks are shown before (*A*) and after (*B*) alignment of the visual stimulus. First-order frequency kernel; left eye, penetration 4/2.

response with the m-sequence by the Fast Walsh Transform (Sutter 1991). This will be called "the first-order response," because it is the impulse response associated with each region of a multi-input *linear* system whose response to the m-sequence most nearly matches the observed response. In qualitative terms, the first-order response is the response to a luminance pulse.

The cross-correlogram also yielded portions of the second-order m-sequence kernel associated with each region, through the relationship $s_n + s_{n+1} \equiv s_{n+4,032} \pmod 2$. (This relationship is specific to the choice of m-sequence, but the existence of relationships of this form is generic.) This response will be called "the second-order off-diagonal response," because it is the near-diagonal slice of the second-order kernel associated with each region of a multi-input *quadratic* system whose response to the m-sequence most nearly matches the difference between the linear approximation and the observed response. In qualitative terms, the second-order off-diagonal response is the response to luminance change (i.e., temporal contrast), independent of sign.

First-order responses from the inverted-repeat runs were negated before averaging with the standard runs. Second-order responses from the inverted-repeat runs were combined with the standard runs without inversion. This maneuver effectively eliminates contamination of odd-order (e.g., linear) and even-order (e.g., second-order) responses. Background on the m-sequence method may be found in Victor (1992).

Lesions and histology

After the recording session, small electrical lesions were made by passing current (5 μA for 5 s) through one or two contacts of the electrode. Responses to checkerboard stimuli were obtained before and after current passage, and if there was no evident change in the field potentials at the site of current passage, additional current (5 μA for 10 s) was passed. At the conclusion of the experiment, the animal was killed with surital, desanguinated with phosphate-buffered saline, and perfused with 4% paraformalde-

hyde. Alternate 40-μm cryostatic sections were stained by the Nissl method, prepared for cytochrome oxidase histochemistry in the standard fashion (Hevner and Wong-Riley 1990), and examined under light microscopy. Histology adequate for identification of electrode penetrations was recovered in five of the seven animals (11 of 16 penetrations).

RESULTS

We report the results of recordings from 16 penetrations in 7 adult male cynomolgus monkeys. In these studies we used a multicontact electrode to sample local field potentials simultaneously at multiple points along a vertical penetration in V1. Our goal was to characterize each penetration in terms of location, size, and ocularity of visual input, spatial tuning, orientation tuning, chromatic tuning, as well as sensitivity to visual form (Purpura et al. 1992). Because we were recording local field potentials rather than isolated single units, we used a range of "noise" stimuli, rather than the standard bars and gratings, to characterize population activity.

Location, size, and ocularity of visual input

The initial recordings at each electrode location were aimed at determining the location of the visual input. In 5 of 16 penetrations, a multiunit response was audible on one or more recording channel. This response was used to line up the center of the visual stimulator with the region of space that elicited the strongest multiunit response, as judged from the audio monitor. In the remaining 11 penetrations, the following procedure was use. As a preliminary step, we recorded the response to flashes or a contrast-reversal checkerboard placed in the region of space correspond-

ing to the back-projected images of the foveae. Then we recorded monocular responses (at the 1 or 2 channels that provided the largest responses to flash or checkerboard) to an array of 249 regions, each modulated by an m-sequence, positioned to cover a 11.5° visual angle. Cross-correlation of the response to the underlying m-sequence revealed which region (or regions) of the stimulus provided a visual input. The visual stimulus was then repositioned to align the center of the stimulus in the location of the peak response for one of the eyes, and this alignment was then verified by a second set of m-sequence stimuli. On a few occasions, the initial m-sequence run failed to elicit responses from either eye. In these cases the CRT was then moved to 57 cm (so that it subtended a 23° visual angle); this maneuver revealed the spatial location of the responses and enabled us to begin the procedure described above. On the basis of the size of the response in the region that provided the largest (peak-to-peak) response to the m-sequence, a "dominant" eye was selected. All further data collection was based on monocular stimulation of this dominant eye. An example of a line-up procedure based on m-sequence stimulation is shown in Fig. 2. All recording locations demonstrated a highly localized retinotopic input, which mapped to within ~5° of the fovea on the tangent screen.

The above procedure not only served the technical need of alignment of the visual stimulus, but also allowed us to estimate the region of visual space that provided input to the recording site. In analogy with the standard notion of the receptive field of a single neuron, we call this region the "population receptive field" (PRF). We estimated the size of the PRF for each eye, by adding the area of each of the stimulus regions that generated a response, weighted by the relative size of the response to that region. For example, the PRF size estimated from the data of Fig. 2B was equal to ~1.8 times the check size: there is a centrally positioned check with a maximal response (1 unit), a check immediately to the right of the maximal response that contributed 0.4 units, a check immediately below the maximal response that contributed 0.3 units, and a check below and to the right that contributed 0.1 units.

We chose this weighting procedure over an unweighted estimate (a count of the regions in which there is a "significant" response) for several reasons. 1) The weighted estimate is minimally influenced by the somewhat arbitrary decision as to whether a region's response was just barely above noise or not, while the unweighted estimate would contribute the full area of the region, or none at all. 2) For PRFs with a sensitivity profile that only asymptotically approached zero (for example, a Gaussian profile), the weighted estimate would provide a number proportional to the peak area at half height, while the unweighted estimate would provide a number independent of the steepness of the decline, but rather limited by the display area. 3) The weighted estimate takes into account the possibility that a response to a region may be small because only a portion of it lies within the PRF. However, the accuracy of any estimate of PRF size from a discrete spatial grid, such as the one we used, is limited by the grid size (typically 0.5 deg^2), and the size of PRFs that are smaller than this grid will be overestimated.

PRF areas were estimated from the first-order kernel and the first off-diagonal slice of the second-order kernel. In both cases, response size was taken as the height (peak-to-peak) of the first major deflection in the kernels derived from m-sequence stimulation. Essentially, the first-order kernel represents a response to local luminance, and the first off-diagonal slice of the second-order kernel represents a response to temporal contrast, independent of the direction of contrast change. The PRF areas ranged from 0.5 to 6.6 deg^2 in both cases. The mean PRF area estimated from the first-order response was slightly larger than the mean PRF area estimated from the second-order response (1.8 vs. 1.5 deg^2, $P = 0.056$ by 2-tailed paired t-test). The peak of the first-order kernel was typically less than that of the second-order kernel (1.7 vs. 2.5 μV, $P = 0.007$ by paired 2-tailed t-test).

Ocular input

In 5 of the 16 penetrations (4 of the 11 penetrations studied with m-sequences), only 1 eye produced significant responses (3 ipsilateral, 2 contralateral). To quantify ocular dominance, we constructed an index as follows: $I_{OD} = (R_{ipsi} - R_{contra})/(R_{ipsi} + R_{contra})$, where R_{ipsi} and R_{contra} indicate the peak-to-peak maximal responses from the ipsilateral and contralateral eyes in response to m-sequence stimulation. Thus a pure contralateral response yielded $I_{OD} = -1.0$, and a pure ipsilateral response yielded $I_{OD} = +1.0$. Intermediate values ranged from -0.29 to 0.41 (1st-order responses) and -0.38 to 0.44 (2nd-order responses). Indices constructed from first- and second-order kernels were highly correlated ($r = 0.96$) with no systematic differences ($P = 0.26$ by 2-tailed paired t-test). The average difference between the I_{OD} calculated from the first-and second-order response (independent of the direction of the difference) was 0.10.

In the seven penetrations with intermediate values of I_{OD} (i.e., those penetrations in which there were responses from both eyes), the PRF tended to have a larger area in the nondominant eye ($P = 0.011$ by 2-tailed paired t-test). This was clearest in measurements from the second-order kernel: (2.6 deg^2 for the nondominant eye, 1.9 deg^2 for the dominant eye, $P = 0.034$ by 2-tailed paired t-test). A similar trend was present for the first-order kernels (2.5 deg^2 for the nondominant eye, 2.2 deg^2 for the dominant eye, $P = 0.19$ by 2-tailed paired t-test). The mean PRF area for the nondominant eye was similar for first- and second-order responses (2.5 vs. 2.6 deg^2, $P = 0.59$ by 2-tailed paired t-test). As was seen for the dominant eye's response, the peak response size for the first-order kernel was less than that for the second-order kernel (1.5 vs. 1.9 μV, $P = 0.039$ by 2-tailed paired t-test). In sum, second-order responses had a smaller spatial spread but a larger peak than first-order responses, and dominant eye responses had a smaller spatial spread but (by definition) a larger peak than nondominant eye responses.

Current source density (CSD) approach

In the rest of the studies presented here, we examined electrical activity at all of the electrode contacts that were in the brain. An example of responses to checkerboard reversal, as measured at 14 adjacent electrode pairs, is shown in Fig. 3A. Many of the channels show similar patterns of activity (channels 8–9 through 11–12, for example). This does not necessarily imply that similar sources are present
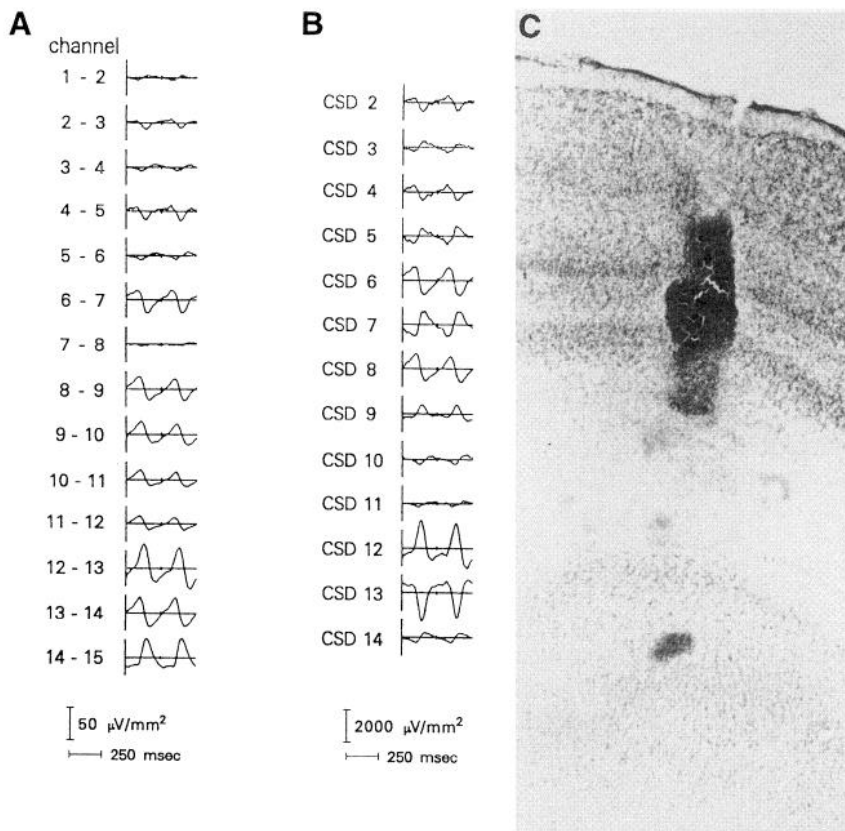
FIG. 3.   *A*: checkerboard reversal responses (1.97 cycle/deg) at each of 14 adjacent contact pairs. *B*: current source density (CSD) estimates derived from these responses. *C*: histological recovery of this penetration (10/2), with a lesion placed at contact 7.

at each of the recording channels, because it is also consistent with a distant field that is simultaneously recorded at each electrode pair. For this reason we transformed these differentially recorded voltages to estimates of current source density (CSD). Because we were interested in optimizing our spatial resolution, we used the three-point formula (Freeman and Nicholson 1975) for the estimate of the second spatial derivative of the field potential.

The three-point formula that transforms referential voltages V_n into an estimate of the second spatial derivative D of voltage at the nth contact is $D = (V_{n-1} - 2V_n + V_{n+1})/h^2$, where h is the intercontact separation. For differential (bipolar) recording, this simplifies to $D = (V_{n-1,n} - V_{n,n+1})/h^2$, where $V_{j-1,j}$ is the voltage $V_{j-1} - V_j$ recorded in bipolar fashion. For unequally spaced contacts, the estimate of the second spatial derivative from voltages V_a and V_b recorded from a triplet of contacts with spacings a and b is

$$D = 2(bV_a - aV_b)/(a^2b + b^2a)$$

This variation was needed to estimate the second spatial derivative at the next-to-last contact, because of the larger spacing between the last two contacts.

CSD estimates derived from these responses are shown in Fig. 3*B*. As is seen from a comparison of Fig. 3*B* with Fig. 3*A*, the CSD estimates indicate that the similar signals seen at channels 8–9 through 11–12 reflect the near absence of a current source at contacts 10 or 11.

After these recordings, an electrical lesion was placed at contact 7. This resulted in an expansion of the histological track over a length of ~200 µm, ending just above the lower border of V1 (Fig. 3*C*). Thus the histology of this penetration indicates that the channels in which CSD estimates were minimal correspond to the white matter underlying V1.

CSD estimates at contacts 2 through 9 reveal multiple distinct phase inversions, reflecting both current sources and current sinks. Because these are steady-state responses, we cannot be sure of whether a positivity of the CSD represents a source or the cessation of a sink. These CSD measurements correspond to electrode contacts within or just below V1. The next two CSD estimates (contacts 10 and 11) are very small and correspond to the portion of the electrode located in the white matter between V1 and the underlying fold of V2. The deepest CSD estimates (channels 12–14) again show prominent sources and sinks and correspond to the portion of the electrode that reached V2.

In all penetrations, CSD estimates obtained from checkerboard responses showed a similar depth profile: six to eight channels at which CSD estimates were large, followed by two or three channels at which CSD estimates were very small. In some cases, there were additional large CSD estimates at the deepest channels (as in Fig. 3). In other cases the second set of large CSD estimates at the deepest channels was not present. When histology was obtained in these cases, the electrode remained in white matter below its exit from V1. Thus the overall pattern of the CSD profile corresponded closely with the traversals of gray matter (multiple large peaks of CSD) and white matter (minimal CSD) and allowed us to identify electrophysiologically the lower border of V1 in those penetrations in which we were unable to recover the penetration histologically.

A control for the multicontact recording technique is illustrated in Fig. 4. Here we estimated CSDs to checkerboard reversal as described above (note the CSD sources and sinks at channels 1–6 and 10–13). Then we advanced the electrode ~1 mm. The pattern of activity seen at CSD channels 5 and 6 after the electrode advance was similar to
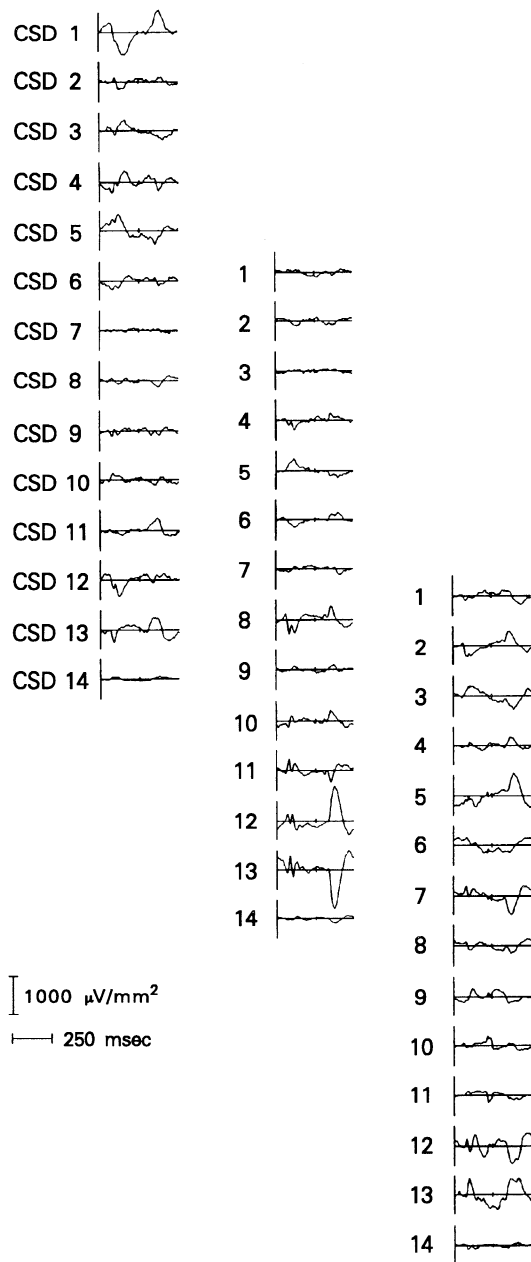
FIG. 4. CSD estimates of checkerboard reversal responses (3.94 cycles/deg) recorded after progressive lowering of the multichannel electrode. Penetration 3/2.

the pattern previously seen at CSD channels 10 and 11. The activity seen at CSD channel 8 after the advance appears to be a mixture of the activity previously present at CSD channels 12 and 13. The activity at CSD channels 10–13 following the advance is new, as would be expected because these channels are now positioned in the space previously occupied by the 1,000-μm gap between the two most distal contacts.

After a second advance of ~ 1 mm, CSD channels 5–7 show activity similar to the activity seen in CSD channels 12 and 13 after the initial advance, and again, a new pattern of activity is seen at CSD channels 9–13. A perfect correspondence of CSD measurements before and after advance of the electrode is not to be expected, because of unavoidable traction of, and damage to, neural tissue. Nevertheless, this control demonstrates that the overall CSD profile was

not an artifact of the recording apparatus (such as impedance differences or gain imbalances), but rather, represents differences in brain activity at multiple depths as sampled by the electrode.

Spatial tuning

In all 16 penetrations, spatial tuning was assessed from responses to samples of Gaussian noise, spatially filtered to restrict power to 1-octave bands. Typical averaged responses to presentations of multiple examples of these stimuli are shown in Fig. 5, A (bipolar recordings) and B (CSD estimates), for the contacts located in V1.

As in the checkerboard responses (Fig. 3, A and B), the similar responses often seen in at neighboring channels in the differential recordings are suppressed in the CSD estimates, because they are consistent with distant generators. Layer-by-layer differences in responses are much more apparent in CSD estimates, and we will therefore focus on the CSD estimates, rather than on the bipolar recordings. There is a systematic dependence of response amplitude on spatial frequency, with a maximal response to the frequency band centered at 1.97 cycle/deg in the upper channels. The dependence on spatial frequency is less prominent in the lower channels (CSD 6 and 7) in terms of amplitude, although there is a clear dependence of response waveform on spatial frequency. This tuning, and the relatively more prominent tuning in the upper layers, was a consistent finding across penetrations.

To compare responses across penetrations, we proceeded as follows. At each penetration, recording sites were selected to represent upper layers and lower layers. For the upper-layer recording, we selected the CSD channel closest to 30% of the way down from the cortical surface to the bottom of V1 (see above and Fig. 3). For the lower-layer recording, we selected the CSD channel closest to 15% of the way up from the bottom of V1. For the penetration whose data are shown in Fig. 5, A and B, this corresponded to CSD 2 for the upper layer, and CSD 6 for the lower layer. Figure 5C shows the dependence of the amplitude of the first harmonic of the CSD, $|F_1|$, on center spatial frequency at these two channels. There is a clear shift from band-pass tuning in the upper layer to low-pass tuning in the lower layer.

Across penetrations and spatial frequencies, the harmonic content of responses changed. Therefore, as an overall response size measure, we chose the quantity

$$A = (|F_1|^2 + |F_2|^2 + |F_3|^2 + |F_4|^2)^{1/2}$$

where F_n is the amplitude of the nth Fourier component of the CSD estimate. As seen in Fig. 5D, this quantity shows the same spatial tuning as does $|F_1|$; however, because it includes amplitudes from several harmonics, it is relatively insensitive to changes in response waveform. Because of the wide variation of peak response amplitudes (39–1,898 μV/mm^2) across recording sites, we used geometric means for descriptive purposes and parametric statistics based on the logarithm of response amplitudes for estimation of statistical significance.

None of the recording sites showed a maximal response to the band-limited noise of highest (center frequency 7.87 cycles/deg) spatial frequency, but many of the sites showed large responses to this stimulus and maximal responses to
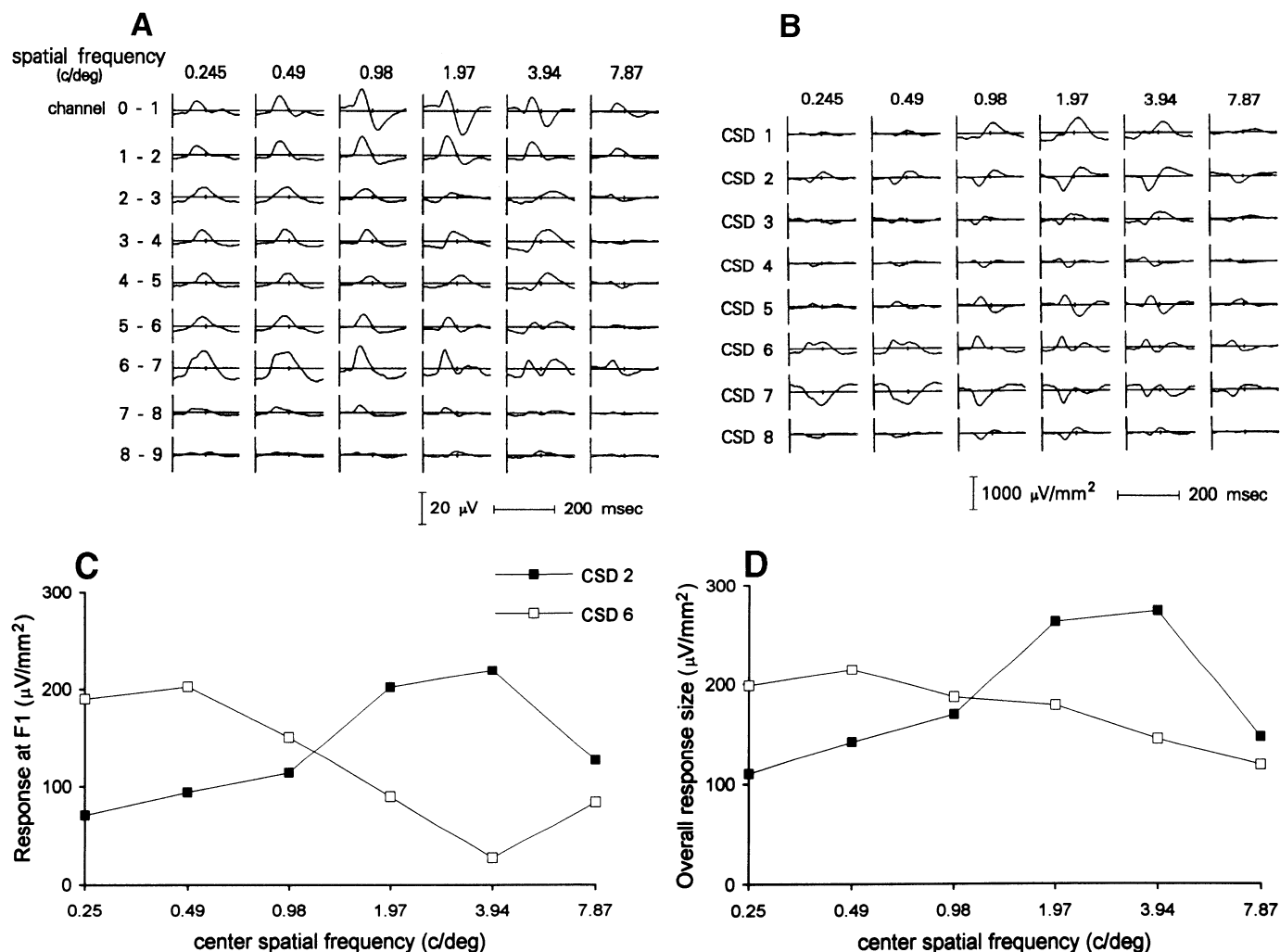
FIG. 5. Responses to luminance modulation of band-limited noise stimuli. *A*: differentially recorded voltages at each of 9 pairs of adjacent contacts (units: μV). *B*: CSD estimates. *C*: dependence of $|F_1|$, the amplitude of the 1st harmonic, on center spatial frequency for CSD estimates from a representative upper-layer contact (CSD 2) and a representative lower-layer contact (CSD 6). *D*: dependence of the composite amplitude measure $A = (|F_1|^2 + |F_2|^2 + |F_3|^2 + |F_4|^2)^{1/2}$ on center spatial frequency. Penetration 7/2.

the stimulus one octave lower. The ratio of the response at this frequency (3.94 cycles/deg) to the response at the lowest spatial frequency (0.245 cycle/deg) was therefore taken as an index of the depth of spatial tuning. In the upper layers, this ratio ranged from 0.73 to 7.3; in the lower layers, this ratio ranged from 0.24 to 5.7. There was a consistent finding of more prominent spatial tuning in the upper layers (geometric mean 2.0 vs. 1.2, $P = 0.0092$ by 2-tailed paired *t*-test). Responses in the upper layers and lower layers were of comparable size at the lowest spatial frequency (geometric mean 123 vs. 110 μV/mm^2, $P = 0.85$), but at 3.94 cycles/deg, responses were substantially larger in the upper layers (geometric mean 248 vs. 133 μV/mm^2, $P = 0.020$ by 2-tailed paired *t*-test). These findings did not depend on the particular choice (0.245 cycle/deg) of the low spatial frequency; similar results were obtained from the responses at 0.49 cycle/deg.

The peak spatial frequency (assessed by quadratic fits to the log-amplitude vs. log-spatial frequency curves) had a mean of 1.8 cycle/deg in the upper layers, and 1.1 cycle/deg in the lower layers ($P = 0.0068$ by 2-tailed paired *t*-test). Thus several measures indicated a shift in spatial tun-

ing from a generally band-pass character in the upper layers to a generally low-pass character in the lower layers, with less low-frequency attenuation and also a lower spatial-frequency cutoff. These differences were not accompanied by any difference in the overall size of the peak response (geometric mean 287 vs. 210, $P = 0.16$ by 2-tailed paired *t*-test). Of note (Fig. 6), the peak spatial frequency of the response was negatively correlated with PRF size in the lower layers ($r = -0.479$, $P = 0.048$) but not in the upper layers ($r = -0.10$).

Checkerboard responses

In 15 penetrations, spatial tuning was also assessed from responses to contrast–reversing checkerboards across check sizes ranging from 1.43 to 0.089°, corresponding to spatial frequencies (along the diagonal) of 0.49 to 7.87 cycles/deg. Typical responses are shown in Fig. 7. The most prominent finding in Fig. 7 is that responses to the two phases of contrast reversal are nearly identical for small checks but become different as the check size becomes larger. That is, the antisymmetric response component (Fig. 7*B*), constructed from the odd harmonics of the CSD
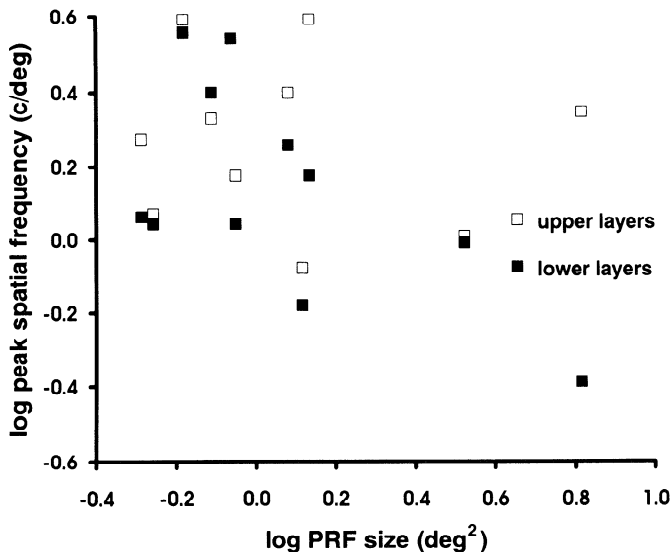
FIG. 6. Relationship of population receptive field (PRF) size, as estimated from the 1st-order kernel, to peak spatial frequency of response. There was a significant correlation for lower layers (■) but not for upper layers (□).

estimates, are essentially absent at high spatial frequencies but become a significant contributor to the response at low spatial frequencies.

A fully symmetric response implies either an intrinsic symmetry in responses to luminance increments and decrements or a PRF sufficiently large so that it includes equal input from bright and dark checks in the stimulus. A response asymmetry implies not only an unequal response to luminance increment and decrement, but also a check size sufficiently large so that the PRF receives unequal inputs from the bright and dark checks. The symmetry of the response was quantified by the ratio constructed from the amplitude

$$A_{even} = (|F_2|^2 + |F_4|^2 + |F_6|^2 + |F_8|^2)^{1/2}$$

of the first four even harmonics and the amplitude

$$A_{odd} = (|F_1|^2 + |F_3|^2 + |F_5|^2 + |F_7|^2)^{1/2}$$

of the first four odd harmonics

$$I_{SYM} = (A_{even} - A_{odd})/(A_{even} + A_{odd})$$

In most cases, contributors $F_1, \ldots, F_7$ to the antisymmetric response components (A_{odd}) were not significantly different from zero at 3.94 cycles/deg by the T_{circ} statistic ($I_{SYM} = 1$). Over all penetrations, the symmetry index calculated from upper-layer responses shifted from 0.88 at 3.94 cycles/deg to 0.50 at 0.49 cycle/deg ($P = 0.0066$ by 2-tailed paired t-test), and in the lower layers, from 0.81 at 3.94 cycles/deg to 0.62 at 0.49 cycle/deg ($P = 0.13$ by 2-tailed paired t-test).

Figure 7C, which isolates the symmetric response component, shows that there is a shift in tuning toward low spatial frequencies in the lower layers. This shift is similar to, but less prominent than, the shift seen for band-limited noise (Fig. 5). Note that again there is a prominent change in the response waveforms at CSD channels 6 and 7 as spatial frequency varies.

To compare tuning across layers, and to compare tuning with that seen with band-limited noise, we chose the ratio of

the symmetric response size at 3.94 cycles/deg to the symmetric response size at 0.49 cycle/deg as an index of spatial tuning, and used the same spatial and temporal frequencies for the band-limited noise responses. Checkerboard responses showed an overall shift to lower spatial frequencies in the lower layers (ratio of 1.19 in upper layers, 0.93 in the lower layers), but this difference was not significant ($P = 0.087$ by 2-tailed paired t-test). The band-pass spatial tuning of the upper layers was less evident for checkerboards than for band-limited noise (ratio of 1.84 for band-limited noise vs. 1.19 for checkerboards, $P = 0.0069$ by 2-tailed paired t-test). The less-prominent spatial tuning seen with checkerboard patterns is most likely a consequence of the
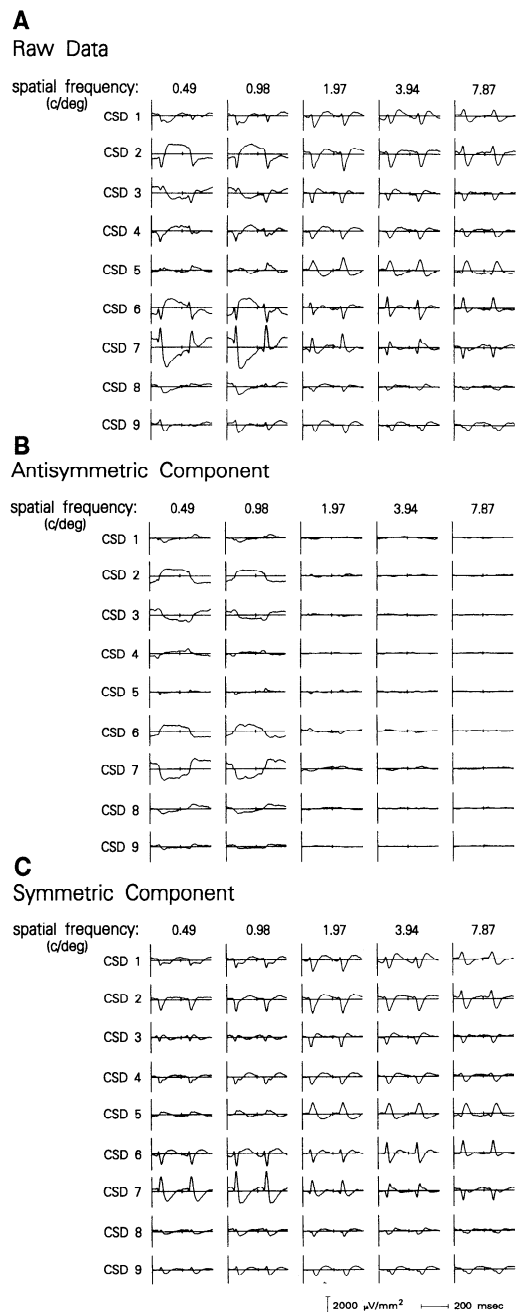

FIG. 7. Responses to checkerboard contrast-reversal stimuli. A: CSD estimates. B: antisymmetric component, constructed from the odd harmonics of the CSD estimates. C: symmetric component, constructed from the even harmonics of the CSD estimates. Penetration 7/2.

presence of low spatial frequencies even in a small-check checkerboard.

Orientation tuning

In 12 penetrations, orientation tuning was assessed by responses to band-limited Gaussian noises further filtered to remove all orientations except those within a 45° wedge (e.g., Fig. 1B). We chose the spatial frequency band of the noise to be just below the optimal spatial frequency in the upper layers, so that the stimulus activated both upper and lower layers. An example of the CSD estimates elicited by these anisotropic band-limited noise stimuli are shown in Fig. 8A. In CSD channels 5, 6, and 7, there is a clear qualitative dependence of the response on the stimulus orientation, with single-peaked waveforms at orientations 45–90°, but more complex waveforms at other orientations. We measured the Fourier components of the CSD at the representative upper and lower layer contacts that were chosen for the analysis of spatial-frequency tuning. Figure 8, B and C, shows the amplitude of the response at the fundamental, $|F_1|$, and the second harmonic, $|F_2|$, for the data of Fig. 8A. At CSD 5, there is a strong but reciprocal dependence of these measures on orientation. That is, as a function of stimulus orientation, response varied not only in magnitude but also in waveform.

We analyzed the dependence of response on orientation in three ways. The first strategy, based on a traditional notion of orientation tuning, was predicated on the assumption that orientation-tuning would be manifest on a sinusoidal variation of some measure of response size on orientation. That is, for each orientation θ, we calculated an overall response size

$$A(\theta) = (|F_1|^2 + |F_2|^2 + |F_3|^2 + |F_4|^2)^{1/2}$$

from the first four Fourier components of the response, and then compared the average response across orientations

$$A_{\text{unoriented}} = \langle A(\theta) \rangle$$

with the quantity

$$A_{\text{oriented}} = 2|\langle A(\theta) \exp(-\pi\iota\theta) \rangle|$$

Here $A_{\text{unoriented}}$ estimates the average response size, and A_{oriented} estimates the orientation dependence of the response size, under the assumption that it depends sinusoidally on the orientation θ. A value of the index $I_{\text{ORIENT,SIZE}} = A_{\text{oriented}}/A_{\text{unoriented}}$ of 0 indicates that response is independent of orientation. A value of 1 would be obtained if response depended sinusoidally on orientation, with no response orthogonal to the preferred orientation. Measured by $I_{\text{ORIENT,SIZE}}$, orientation tuning ranged from 0.04 to 0.38 in the upper layers and 0.08 to 0.39 in the lower layers (means of 0.18 vs. 0.24, $P = 0.49$ by 2-tailed t-test). For the data of Fig. 8, this index was 0.15 (upper layer) and 0.22 (lower layer).

The second index of orientation tuning was based on response dynamics, rather than response size. As a crude measure of response dynamics, we used the quantity

$$Q(\theta) = 1 - |F_1|/(|F_1|^2 + |F_2|^2 + |F_3|^2 + |F_4|^2)^{1/2}$$

which ranges from 0 for a response entirely contained in the 1st harmonic to 1 for a response that is entirely contained in the higher harmonics. Figure 8D shows an example of how this measure depends on orientation.

The orientation tuning of $Q(\theta)$ was measured by comparing its average across all orientations

$$Q_{\text{unoriented}} = \langle Q(\theta) \rangle$$

with

$$Q_{\text{oriented}} = 2|\langle Q(\theta) \exp(-\pi\iota\theta) \rangle|$$

The index $I_{\text{ORIENT,DYN}} = Q_{\text{oriented}}/Q_{\text{unoriented}}$ has a significance analogous to that of $I_{\text{ORIENT,SIZE}}$, except that response dynamics, rather than response size, is compared across orientations. Measured by $I_{\text{ORIENT,DYN}}$, orientation tuning ranged from 0.04 to 0.75 in the upper layers and 0.10 to 0.90 in the lower layers (means of 0.25 vs. 0.35, $P = 0.42$ by 2-tailed paired t-test). For the data of Fig. 8, the value of this index was 0.36 (upper layer) and 0.32 (lower layer). Orientation tuning as manifest by $I_{\text{ORIENT,DYN}}$ was well-correlated with orientation tuning as manifest by $I_{\text{ORIENT,SIZE}}$ ($r = 0.57$, $P = 0.008$), but $I_{\text{ORIENT,DYN}}$ was significantly larger than $I_{\text{ORIENT,SIZE}}$ ($P = 0.010$ across all layers by 2-tailed paired t-test). That is, orientation tuning was manifest more strongly in the response dynamics than in its overall size.

The third strategy to analyze orientation tuning determines whether the variability of responses across orientations is larger than that expected from the variability of responses within orientations, but does not make any assumptions concerning how response depends on orientation. In contrast to the first two strategies, which were based solely on response amplitudes, this strategy is sensitive to response phase.

The analysis proceeds in a frequency-by-frequency manner and makes use of the individual responses to each 15-s trial, as well as the average response across trials. Having chosen a frequency of interest, we use $z_{j,\theta}$ to represent the complex Fourier component of the estimated current source density measured in the jth trial for the orientation θ. These quantities are averaged vectorially to calculate $z_{\theta,\text{mean}}$, the average response to noises of orientation θ. The response variance V_θ for this orientation is then estimated by

$$V_\theta = (\sum_j |z_{j,\theta} - z_{\theta,\text{mean}}|^2)/(N_\theta - 1)$$

where N_θ is the number of trials for the orientation θ. Together, the individual variances for each orientation V_θ are combined to form a within-condition variance

$$V_{\text{within}} = [\sum (N_\theta - 1)V_\theta]/[\sum (N_\theta - 1)]$$

where the summations are over all orientations θ.

We also calculate a response variance V_{across} across all orientations, given by

$$V_{\text{across}} = [\sum N_\theta |z_{\theta,\text{mean}} - z_{\text{across}}|^2]/(N - 1)$$

where z_{across} is the (vector) average of responses across all orientations and N is the number of orientations. Under the null hypothesis that there is no dependence on orientation, the two variance estimates V_{across} and V_{within} will be identical. Conversely, a dependence of response on orientation would be manifest by excess variance across orientations; that is, a ratio

$$R = V_{\text{across}}/V_{\text{within}}$$

significantly greater than 1. The ratio R is distributed as an F-statistic whose numerator has $2(N - 1)$ degrees of freedom and whose denominator has $2 \sum (N_\theta - 1)$ degrees of

freedom (Victor and Mast 1991). Essentially, this approach is an analysis of variance for complex-valued quantities (the Fourier components).

In all of the 12 penetrations examined, there was a significant ($P < 0.05$) dependence of response on orientation, as manifest by the variance ratio R calculated from at least one of the first four harmonics of the response. In eight of these penetrations, these values were highly significant ($P < 0.005$), and there were significant values of the variance ratio R in both upper and lower layers. Two of the penetrations had significant values of R just in the upper layers, and two had significant values just in the lower layers. In the data shown in Fig. 8, significance levels for upper-layer (CSD 1) responses were $P = 0.25$ (F1) and $P < 0.01$ (F2); significance levels for lower-layer (CSD 5) responses were $P < 0.003$ (F1) and $P < 0.02$ (F2).

Because R is calculated on a frequency-by-frequency basis, we could determine which temporal frequencies contained responses that were most dependent on orientation. To compare across penetrations and layers, we transformed R into

$$H = -\ln [p(R)]$$

where $p(R)$ is the significance level of R, as calculated from the appropriate F-distribution.

H may be regarded as an information rate, for the following reason. Assume that k successive sets of presentations yield similar responses, each with variance ratio R and significance level p (near 0). Because p represents the probability that the orientation dependence within each set of observations was due to chance alone, then the probability that all observations were due to chance alone is approximately p^k. According to the formula $H = -\ln [p(R)]$, the value of H for the combined sets of presentations is related to the value of H for the individual presentations by $H_{\text{combined}} = kH_{\text{indiv}}$. That is, higher levels of statistical significance or longer observation times contribute multiplicatively to H. More concretely, a value of $H = 4$ implies a high level of significance [$P = e^{-4}$ (~ 0.018)] within the observed set of data. Doubling the value of H thus indicates that a very high level of significance [$P = e^{-8}$ (~ 0.00034)] within the observed set of data, or, equivalently, significance at the level of e^{-4} from a typical half of the observed data. Because all datasets comprised approximately the same length, normalization of H for dataset length is not necessary.

The dependence of the average value of H on temporal frequency is shown in Fig. 9. We did not find significant differences between values of H between upper and lower layers at any temporal frequency, and they are therefore pooled in this analysis. Values of H are highly significant for the first and second harmonics (4.2 and 8.4 Hz), borderline at the third harmonic (12.7 Hz), and insignificant at higher temporal frequencies. For comparison, a similar analysis was performed for spatial-frequency tuning. The overall values of H were approximately twofold higher, but the dependence of H on temporal frequency was comparable.

Chromatic tuning

In nine of the penetrations, sensitivity to chromatic content was assessed by responses to isotropic band-limited Gaussian noises presented with counterphase modulation of the R and G CRT guns. In these experiments, R modula-

tion was held fixed at maximal (standard deviation of 0.4 across the stimulus), and counterphase G modulation was stepped through a range of G/R ratios: 0, 0.1, 0.25, 0.3, 0.312, 0.325, 0.333, 0.35, 0.385, 0.4, 0.5, and 1.0. Calculations based on the emissions of our phosphors and the absorption of the photopigments (Baylor et al. 1987; Smith and Pokorny 1975) provided the following critical counterphase G/R ratios: L-cone silencing at a ratio of 0.385, M-cone silencing at a ratio of 0.15, and photometric isoluminance at a ratio of 0.30. The spatial frequency of the stimulus was chosen to be one octave below the peak spatial frequency for responses to achromatic band-limited noise (0.245–1.97 cycles/deg).

An example of the CSD estimates elicited by these stimuli are shown in Fig. 10. Responses were generally smaller than responses elicited by luminance modulation and are nearly absent in some channels. Responses in CSD channels 4 and 5 are attenuated to stimuli that are near photometric isoluminance. All harmonics are less than one-half of the estimated confidence limit (i.e., not significantly different from 0) at the G/R ratio of 0.3. At G/R ratios ≤ 0.25 or ≥ 0.35, they are small but significant (by the T_{circ} statistic). However, the response size does not simply depend on luminance. In CSD channels 4 and 5, the responses have a simple waveform when the M cone modulation is small (counterphase G/R ratios from 0 to 0.25), and a more complex waveform when the M cone modulation is large and in phase with luminance (counterphase G/R ratios of 0.6 or 1.0). Furthermore, upper-layer responses (CSD channels 1 and 2) did not null at isoluminance or at either of the cone-silencing ratios.

We developed two kinds of indices to express dependence of response on chromatic content. The first kind of index was based on a model of how response might depend on chromatic content, analogous to the indices $I_{\text{ORIENT,SIZE}}$ and $I_{\text{ORIENT,DYN}}$ introduced for orientation tuning. The model is based on the notion of distinct, possibly nonlinear, chromatic mechanisms whose outputs are combined linearly. In the model, the chromatic mechanisms M_1, M_2, . . . have chromatic sensitivities defined by an array M_{mu}, where M_{mu} is the sensitivity of the mechanism M_m to modulation of CRT primary u (u = R, G, or B). The response of the mechanism M_m to a chromatic stimulus S_a (characterized by modulations along the CRT primaries u of S_{ua}) is given by Q_{ma}, where

$$Q_{\text{ma}} = F_m(M_{\text{mR}}S_{\text{Ra}} + M_{\text{mG}}S_{\text{Ga}} + M_{\text{mB}}S_{\text{Ba}})$$

Because our stimuli are counterbalanced for positive and negative contrast (through the design of the underlying Gaussian noises), only even-symmetrical components of the function F_m can contribute to a response. On the basis of both the need for simplicity and the prevalence of rectification in cortical neurons, we make the assumption that F_m is full-wave rectification, as suggested by Lennie et al. (1990). That is

$$Q_{\text{ma}} = | M_{\text{mR}}S_{\text{Ra}} + M_{\text{mG}}S_{\text{Ga}} + M_{\text{mB}}S_{\text{Ba}} |$$

(We also used functions $F_m(x) = |x|^\alpha$ for exponents α in the range 0.5–2.0; choices within this range did not result in a consistent or significant improvement in the model fits described below.)

We furthermore assume that each mechanism M_m has a

response whose dynamics are characterized by a Fourier component D_{fm} at the frequency f, scaled by the overall response size Q_{ma}. Thus the predicted response $z_{fa,pred}$ at the frequency f to a stimulus S_a is given by a summation over all mechanisms m

$$z_{fa,pred} = \sum_m D_{fm}Q_{ma}$$

To specify the model, we postulate a set of sensitivities M_{mu} for the chromatic mechanisms. The dynamics D_{fm} are adjusted to minimize the unexplained variance $\sum_f \sum_a |z_{fa,pred} - z_{fa,obs}|^2$. With M_{mu} and F_m fixed, this problem essentially is a linear least-squares fit, and the explained variance has the simple matrix expression

$$V_{expl} = \text{tr}\,[Q^T(QQ^T)^{-1}Qz^Tz]$$

Initially, we chose a model based on the three cardinal chromatic mechanisms: a luminance mechanism, and the two purely chromatic mechanisms L-M and S (Derrington et al. 1984; Lennie et al. 1990). We give combined statistics across upper and lower layers, because there were no significant differences at these sites. This three-mechanism model explained an average of 75.0% of the variance (range: 53.2–96.4%) in the first four harmonics. Although we could not exclude the possibility of systematic departures from the model in the remaining 25% of unexplained variance, this residual variance was comparable with the uncertainty in the measured responses. A model based on three cone-isolating mechanisms explained significantly less of the variance (70.6%; range: 39.1–88.9%, $P = 0.042$ 1-tailed paired t-test). Both of these models have the same number of free parameters (the implicitly estimated Fourier components of the responses to hypothetical stimuli that drive only a single mechanism), and thus it is the choice of mechanisms, not a change in the number of parameters, that must account for the difference between them.

We then determined to what extent all three chromatic mechanisms of the cardinal-mechanism model were required to account for the variance. Removal of the S-cone mechanism from the model eliminated an average of only 15.7% of the total explained variance (range: 2.6–34.1%).

A two-mechanism model based on luminance and (L-M) mechanisms only accounted for 64.0% of the total variance (range: 35.0–91.8%). The luminance mechanism and the (L-M) mechanism contributed approximately equally to the variance explained by the two-mechanism model. The luminance mechanism alone accounted for 74.1% of its variance (range: 42.1–98.6%); the (L-M) mechanism alone accounted for 70.2% of its variance (range: 31.8–93.2%). This approach formalizes the qualitative observation made from Fig. 10 that luminance alone fails to account for the dependence of dynamics on chromatic content. Note that the variances explained by each mechanism alone do not add up to the variance explained by the combined model, because the mechanisms are not orthogonal for the set of experimental color directions. This nonorthogonality is expressed by the matrix $Q^T(QQ^T)^{-1}Q$.

The second approach to assessment of chromatic sensitivity was through the variance ratio $R - V_{across}/V_{within}$ described above in connection with orientation tuning. In eight of the nine penetrations examined, there was a significant ($P < 0.05$) dependence of response on chromatic content, as manifest by the variance ratio R calculated from at
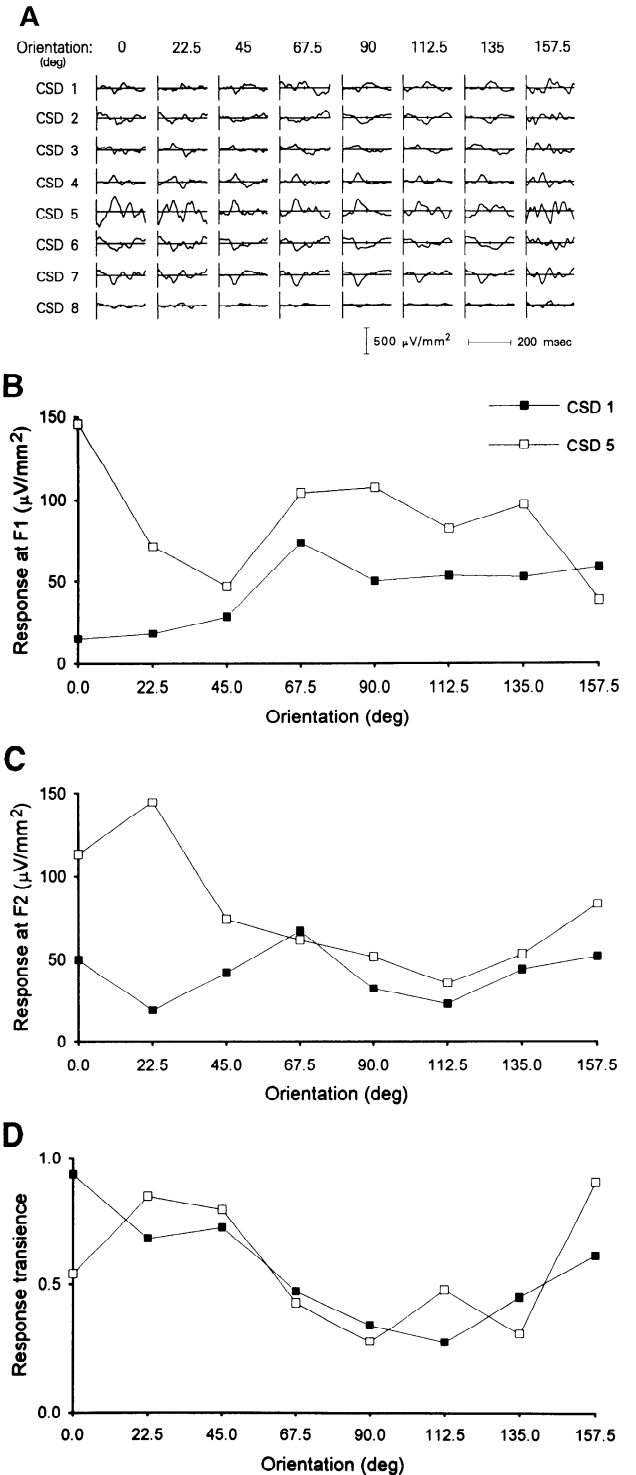

FIG. 8. Responses to oriented band-limited noise centered at 3.94 cycles/deg. A: CSD estimates. Note the dependence of response waveform on orientation in CSD channels 5, 6, and 7. B and C: dependence of the fundamental response (B) and the 2nd harmonic response (C) on orientation for CSD estimates from a representative upper-layer contact (CSD 1) and a representative lower-layer contact (CSD 5). D: dependence of an index of response transience, $Q(\theta) = 1 - |F_1|/(|F_1|^2 + |F_2|^2 + |F_3|^2 + |F_4|^2)^{1/2}$, on orientation. Penetration 4/3.

least one of the first four harmonics of the response. In six of these penetrations, values of R were highly significant ($P < 0.005$). One of the penetrations had significant values of R just in the upper layers, and one had significant values
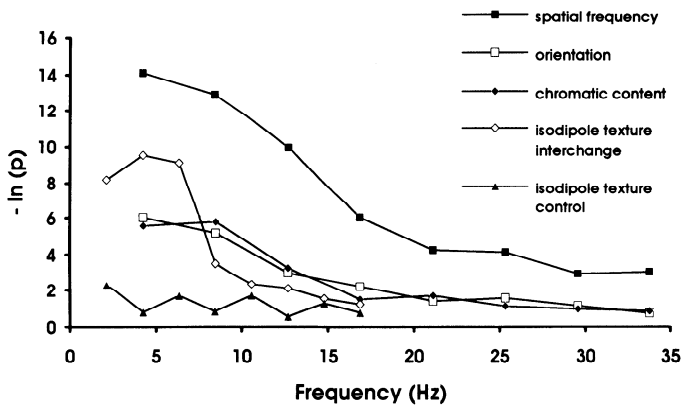
FIG. 9. Dependence of the information rate $H = -\ln p$ on temporal frequency for several stimulus attributes. Spatial frequency (■), orientation (□), chromatic content (♦), and isodipole texture interchange (◇). The ensemble control for isodipole texture interchange (▲) indicates that there is little statistical difference between the responses to different examples drawn from the same isodipole texture class.

just in the lower layers. As seen in Fig. 9, the dependence of information rate on frequency for chromatic content was nearly identical to that seen for orientation tuning.

Responses to near-isoluminant patterns

In five penetrations we compared the spatial tuning of responses to luminance-modulated band-limited noise with the spatial tuning of responses to near-isoluminant (L-M axis) band-limited noise. As is seen in Fig. 11, responses to near-isoluminant noise were much smaller than responses to luminance modulation. At high spatial frequencies (3.94 and 7.87 cycles/deg), it is possible that chromatic aberration introduced significant luminance artifact into the visual stimulus, so that the meaning of the responses at these spatial frequencies is uncertain. However, the most striking finding is that the band-pass characteristic of upper-layer responses to luminance modulation (Fig. 11A) is lost under near-isoluminant conditions (Fig. 11B): there is no attenuation of responses at low spatial frequencies.

The shift in spatial tuning to low spatial frequencies and attenuation of responses at high spatial frequencies was characteristic of the rest of the penetrations. In the upper layers, the index of band-pass tuning (ratio of response size at 3.94 cycles/deg to response size at 0.245 cycles/deg) shifted from 4.34 for luminance modulation to 1.21 for

L-M modulation ($P = 0.021$ by 2-tailed paired t-test). In the lower layers, which had a more low-pass tuning for luminance modulation, there was a further shift to low spatial frequencies at for L-M modulation, but this shift did not reach statistical significance (response ratio of 1.47 for luminance modulation, 0.94 for L-M modulation, $P - 0.16$ by 2-tailed paired t-test).

Responses to low-contrast patterns

In four penetrations, we obtained responses to band-limited Gaussian noise presented at a range of luminance contrasts. Responses, quantified by $A = (|F_1|^2 + |F_2|^2 + |F_3|^2 + |F_4|^2)^{1/2}$, are shown in Fig. 12. At low spatial frequencies (0.49 and 1.97 cycle/deg), responses grow at a rate that is less than proportional to contrast over the entire contrast range [root-mean-square (RMS) contrast 0.025–0.4]. At the high spatial frequency (7.87 cycles/deg), responses grow approximately proportionally to contrast, at least up to an RMS contrast of 0.1. Consequently, the spatial tuning shifts from low-pass at low contrasts to band-pass at high contrasts.

The shift in spatial tuning properties is similar to what was observed (Fig. 11) with near-isoluminant stimuli. On the other hand, the responses to chromatic stimuli (Fig. 10) cannot be explained solely on the basis of their luminance component, because of 1) lack of a null in the upper layers and 2) the dependence of response dynamics on chromatic content, as analyzed above.

DISCUSSION

Summary of results

We have analyzed local field potentials elicited in macaque V1 by a variety of visual stimuli differing in spatial frequency content, orientation, and chromatic balance. Our main findings are as follows. 1) The local field potential has a PRF size of approximately 2 deg^2. 2) In the upper layers, spatial tuning is prominently band-pass. In the lower layers, the band-pass character is less prominent, and there is generally a lower optimal spatial frequency. 3) Orientation tuning was evident in upper and lower layers. Orientation tuning was manifest not only by changes in response size but also by changes in response dynamics. 4) Chromatic tuning was evident in both upper and lower layers. Responses to near-isoluminant stimuli were smaller than
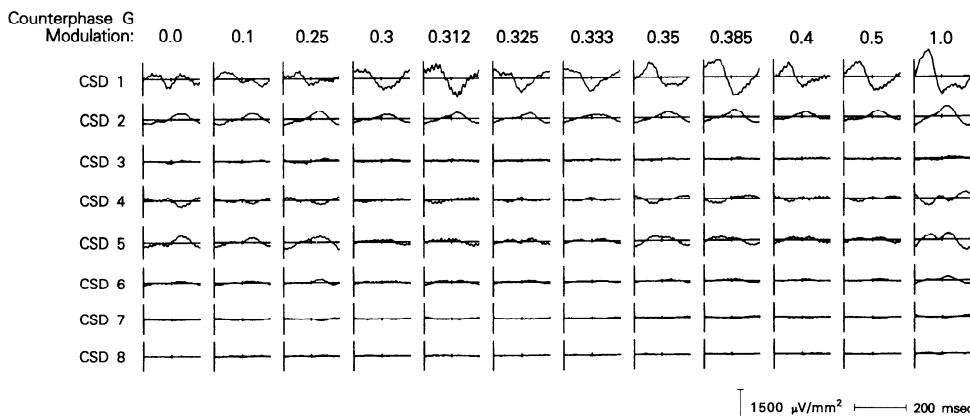

FIG. 10. Responses to chromatic isotropic band-limited noise centered at 0.98 cycle/deg. Responses are attenuated near photometric isoluminance (counterphase G/R ratio of 0.3) in CSD channels 4 and 5. Note the dependence of response waveform on counterphase G modulation for large G/R ratios in these channels. Penetration 5/1.

A
Luminance Modulation
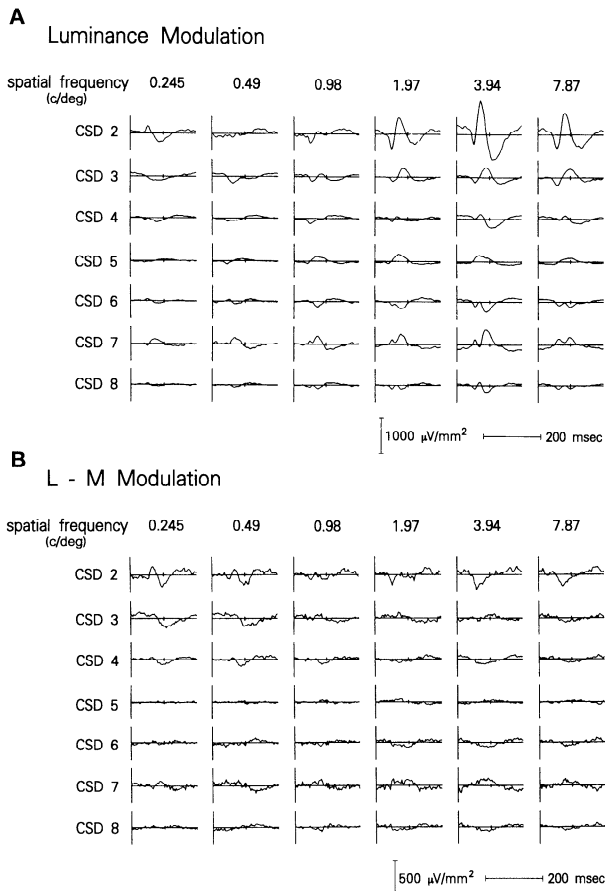

B
L - M Modulation

FIG. 11. Comparison of responses to luminance modulation (A) and L-M modulation (B) of band-limited noise stimuli. Penetration 11/1.

responses to chromatic stimuli. The spatial tuning for these stimuli was low-pass in upper and lower layers and similar to the spatial tuning for low-contrast luminance stimuli. However, the response to stimuli with mixed luminance and chromatic contrast was not governed just by the luminance contrast but displayed a substantial dependence of dynamics on chromatic balance.

Comments concerning CSD estimates and resolution

Our analysis rests on the use of CSD estimates derived from a multicontact microelectrode. We recognize that estimation of CSD from physiological recordings requires an assumption of isotropy of the bulk ohmic properties of the brain, which is at best an approximation (Freeman and Nicholson 1975). The three-point formula for CSD estimates amounts to calculation of successive differences of neighboring bipolar recordings. This removal of signals common to nearby electrodes emphasizes laminar differences (Fig. 5). The CSD estimates show multiple sources and sinks in gray matter but minimal activity in white matter (Fig. 3), which is consistent with the notion that this calculation primarily removes far-field signals.

Our CSD estimates are quoted in units of microvolts per millimeter squared, because we did not include a factor that represents the specific conductivity of the tissue. Freeman and Nicholson (1975) determined the specific resistivity of anuran cerebellum to be 200 Ω-cm; values reported for cor-

tex range from 230 to 350 Ω-cm (Nunez 1981). With this value, our typical CSD estimates of 1,000 $\mu V/mm^2$ correspond to an estimated CSD of 0.3–0.5 mA/cm^3. This is 10- to 100-fold less than the CSDs seen by Freeman and Nicholson (1975), presumably because only a fraction of the neural activity in visual cortex is modulated by the visual stimulus and is sufficiently aligned in space and time to generate a field potential.

It is likely that CSD estimates at each electrode reflect activity in the surrounding 100–150 μm. Along the direction of the penetration, CSD estimates at adjacent channels (150 μm apart) are often quite different (e.g., CSD channels 5, 6, and 7 of Fig. 7). In the lateral direction, no such direct evidence is available. However, the summing distance must be substantially less than 500 μm, because strong ocular dominance was observed in most penetrations. Furthermore, the observation of at least mild orientation tuning in most penetrations implies a summing area whose radius is on the order of an orientation column.

The measured CSD profiles (Figs. 3, 4, 5, 7, 8, 10, and 11) typically showed multiple sources and sinks, thus demonstrating the ability to resolve fine structure within the supragranular and infragranular compartments. However, the detailed laminar patterns differed greatly across penetrations. We cannot determine to what extent these differences are due to physiological differences across penetrations (e.g., Tootell et al. 1988) or simply an undersampling of cortical structure by the resolution of the recording apparatus (150-μm intercontact distance).

To compare activity across penetrations, we chose representative channels in the upper and lower portions of V1. We found substantial differences in spatial tuning, orientation tuning, and chromatic sensitivity across penetrations, but no striking correlations among these variations (Table 1). However, even with this relatively crude view of the columnar activity profile and the limited number of penetrations, substantial differences between upper and lower layers did emerge, primarily in the domain of spatial tuning. Although a greater resolution would certainly be desirable, the subdivision of cortex into a supragranular and an infragranular compartment appears to be a fundamental one for understanding the organization of cortical computational mechanisms (Douglas and Martin 1991).
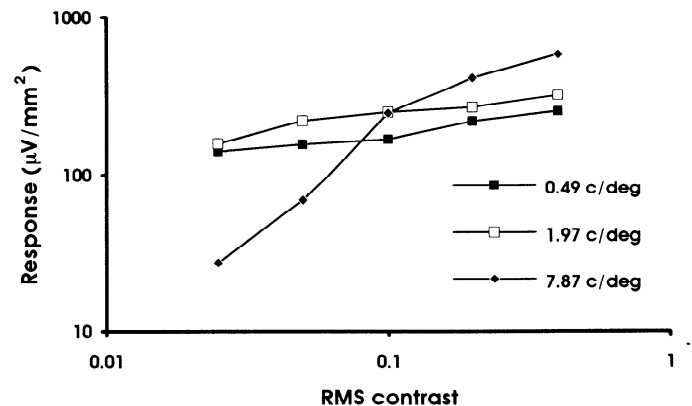

FIG. 12. Response to luminance modulation of band-limited noise at a range of contrasts. Response size is quantified by $A = (|F_1|^2 + |F_2|^2 + |F_3|^2 + |F_4|^2)^{1/2}$, where $|F_j|$ is the amplitude of the jth harmonic of the CSD estimate. Penetration 11/1.

TABLE 1.   *Correlations among tuning for spatial frequency, orientation, and color*

	Upper Layers	Lower Layers	Combined
Spatial frequency tuning vs. orientation tuning	−0.06	−0.08	−0.15
Spatial frequency tuning vs. chromatic tuning	0.18	−0.12	0.11
Orientation tuning vs. chromatic tuning	−0.20	0.45	0.07

Correlations among indices of spatial tuning, orientation tuning, and chromatic tuning across penetrations and recording sites. The indices used (see text) are spaital tuning, log [(response at 3.94 cycles/deg)/(response at 0.245 cycle/deg)]; orientation tuning, $I_{ORIENT,DYN}$; chromatic tuning, fraction of variance explained by addition of an L-M mechanism to a luminance-only model (see text for model details). None of these correlations are significant at $P = 0.10$ (2-tailed).

Encoding of stimulus attributes in response dynamics

We determined tuning of neural responses to spatial frequency, orientation, and color by comparing population responses to multiple examples of random stimuli. This approach contrasts with the traditional approach of determination of tuning through stimuli optimally positioned for the response of a single neuron in that it emphasizes the population response, which is likely dominated by the vast majority of neurons for which the visual stimulus is not optimal. Nevertheless, the phenomena of spatial tuning, orientation tuning, and chromatic tuning that are well-established through the study of single units stimulated with optimally positioned bars and gratings (De Valois and De Valois 1988; Hubel and Wiesel 1977; Lennie et al. 1990) are readily apparent in the population responses to noise stimuli.

One striking feature of our recordings is that stimulus attributes are encoded in the dynamics of the population responses, and not just in the overall size of this response. We examined the nature of temporal coding across stimulus attributes through a statistical measure of information rate. The information rate statistic (Fig. 9) compares the responses to multiple examples of noise stimuli that differ in a single attribute, such as spatial frequency, orientation, or chromatic balance. Because information rate was calculated separately for each harmonic in the response, it is possible to determine which components of the response dynamics convey information about each response attribute. For spatial frequency, information is distributed in the response dynamics across a broad temporal frequency range, including the range 4–25 Hz. Orientation tuning and chromatic tuning share a nearly identical dependence of information rate on temporal frequency. In each case there is a gradual decline of information rate with temporal frequency, and the information rate remains significant up to 13 Hz. The information rate for orientation and chromatic tuning is approximately one-half of that seen for spatial frequency tuning across all temporal frequencies. That is, the difference between these stimulus attributes appears to be one of overall efficiency, rather than differences at specific temporal frequencies.

This similar dependence of information content on temporal frequency that we have seen for these "classical" attributes of spatial frequency, orientation, and color stands in striking contrast to the dependence of information content on temporal frequency for a more complex attribute. In psychophysical and visual evoked potential studies (Victor and Conte 1989, 1991), we used isodipole textures (Julesz et al. 1978) to separate nonlinear processes underlying form processing from spatial filtering. Isodipole texture en-sembles are readily distinguishable on the basis of local elements of form, but share the same power spectrum (either measured as a spatial average or an ensemble average). We have shown that V1 neurons are able to distinguish between these textures (Purpura and Victor 1990) and that these discriminations are manifest at the level of the local field potential (Purpura et al. 1992, 1994). The frequency dependence of the information rate in these texture responses is also shown in Fig. 9. These information-rate data were derived from isodipole texture responses obtained at the same recording sites as those used in the present study, with comparable contrasts, spatial frequencies, and analysis periods (Purpura et al. 1992, 1994). The difference between frequency dependence of the information rate for texture discrimination and for the classical attributes is not one of simply an overall difference in efficiency. Rather, for texture discriminations, the information rate is disproportionately high at low temporal frequencies.

Thus our studies of population responses to a variety of visual stimuli reveal that classical stimulus attributes (spatial frequency, orientation, and color) are encoded at least in part in the response dynamics. The frequencies used for the encoding, however, are not a fixed property of visual cortex. Rather, as seen by a comparison with isodipole texture responses, the frequencies used for temporal coding depend on the stimulus attribute.

Although temporal coding is not a widely emphasized feature of visual processing, it has been identified in single-unit studies of retinal output (McClurkin et al. 1991b), the thalamus (McClurkin et al. 1991a), V1 (McClurkin et al. 1991b), and extrastriate cortex (Richmond et al. 1987). Our findings add to these single-unit studies in several important ways.

We have shown that temporal encoding occurs at the level of the local neural population. That is, population encoding of stimulus attributes is a robust phenomenon, which does not depend on selectively observing the response of a single neuron to an optimally positioned stimulus.

Second, our studies were done under steady-state conditions, so that responses were not dominated by a contrast transient. With transient stimuli, the response waveform may be dominated by an overall response to temporal contrast. Temporal encoding for overall contrast changes is to be expected on the basis of retinal mechanisms alone, simply as a consequence of the well-known differences in dynamics between center and surround mechanisms (Enroth-Cugell and Pinto 1972; Ratliff et al. 1969). More generally, the temporal coding we observe is unlikely to be due to subcortical mechanisms, because *1*) it encodes orientation

(Fig. 8) and 2) it includes the generation of higher harmonics for specific chromatic inputs (Fig. 10).

Most importantly, we have shown that temporal encoding depends on which stimulus attribute is encoded. For spatial frequency, orientation, and color, information is carried at different overall rates, but over a similarly wide frequency range. For texture discrimination, information is carried more heavily in the lower temporal frequencies. This demonstrates that the way that information is carried in the population firing pattern is not a consequence of intrinsic population dynamics but is stimulus driven.

REFERENCES

BAYLOR, D. A., NUNN, B. J., AND SCHNAPF, J. L. Spectral sensitivity of cones of the monkey *Macaca fascicularis*. *J. Physiol. Lond.* 390: 145–160, 1987.

DERRINGTON, A. M., KRAUSKOPF, J., AND LENNIE, P. Chromatic mechanisms in lateral geniculate nucleus of macaque. *J. Physiol. Lond.* 357: 241–265, 1984.

DE VALOIS, R. L. AND DE VALOIS, K. K. *Spatial Vision*. New York: Oxford Univ. Press, 1988.

DOUGLAS, R. J. AND MARTIN, K. A. C. A functional microcircuit for cat visual cortex. *J. Physiol. Lond.* 440: 735–769, 1991.

ENROTH-CUGELL, C. AND PINTO, L. Properties of the surround response mechanism of cat retinal ganglion cells and center-surround interaction. *J. Physiol. Lond.* 220: 403–439, 1972.

FREEMAN, J. A. AND NICHOLSON, C. Experimental optimization of current source density technique for anuran cerebellum. *J. Neurophysiol.* 38: 369–382, 1975.

HEVNER, R. F. AND WONG-RILEY, M. T. T. Regulation of cytochrome oxidase protein levels by functional activity in the macaque monkey visual system. *J. Neurosci.* 10: 1331–1340, 1990.

HUBEL, D. H. AND WIESEL, T. N. Ferrier lecture. Functional architecture of macaque monkey visual cortex. *Proc. R. Soc. Lond. B Biol. Sci.* 198: 1–59, 1977.

JULESZ, B., GILBERT, E. N., AND VICTOR, J. D. Visual discrimination of textures with identical third-order statistics. *Biol. Cybern.* 31: 137–149, 1978.

KATZ, E., PURPURA, K., MAO, B., SCHROEDER, C., AND VICTOR, J. D. Responses to broad-band and band-limited noise in V1: dependence on spatial frequency, color and orientation. *Soc. Neurosci. Abstr.* 18: 295, 1992.

LENNIE, P., KRAUSKOPF, J., AND SCLAR, G. Chromatic mechanisms in striate cortex of macaque. *J. Neurosci.* 10: 649–669, 1990.

LEVENTHAL, A. G., THOMPSON, K. G., LIU, D., NEUMAN, L. M., AND

AULT, S. J. Form and color are not segregated in monkey striate cortex (Abstract). *Invest. Ophthalmol. Visual Sci.* 34, *Suppl.*: 813, 1993.

LIVINGSTONE, M. S. AND HUBEL, D. H. Anatomy and physiology of a color system in the primate visual cortex. *J. Neurosci.* 4: 309–356, 1984.

MCCLURKIN, J. W., GAWNE, T. J., OPTICAN, L. M., AND RICHMOND, B. J. Lateral geniculate neurons in behaving primates. II. Encoding information in the temporal shape of the response. *J. Neurophysiol.* 66: 794–808, 1991.

MCCLURKIN, J. W., OPTICAN, L. M., RICHMOND, B. J., AND GAWNE, T. J. Concurrent processing and complexity of temporally coded messages in visual perception. *Science Wash. DC* 253: 675–677, 1991.

MILKMAN, N., SCHICK, G., ROSSETTO, M., RATLIFF, F., SHAPLEY, R., AND VICTOR, J. D. A two-dimensional computer-controlled visual stimulator. *Behav. Res. Methods Instrum.* 12: 283–292, 1980.

NUNEZ, P. L. *Electric Fields of the Brain*. New York: Oxford Univ. Press, 1981.

O'KEEFE, L. P., LEVITT, J. B., KIPER, D. C., SHAPLEY, R. M., AND MOVSHON, J. A. Functional organization of owl monkey LGN and visual cortex. *Invest. Ophthalmol. Visual Sci.* 34, *Suppl.*: 907, 1993.

PURPURA, K., KATZ, E., MAO, B., CANEL, A., AND VICTOR, J. D. Responses to broad-band and texture stimuli in V1: evidence for spatial and temporal interactions. *Soc. Neurosci. Abstr.* 18: 295, 1992.

PURPURA, K., TRANCHINA, D., KAPLAN, E., AND SHAPLEY, R. M. Light adaptation in the primate retina: analysis of changes in gain and dynamics of retinal ganglion cells. *Visual Neurosci.* 4: 75–93, 1990.

PURPURA, K. AND VICTOR, J. D. Processing of form in monkey visual area V1. *Soc. Neurosci. Abstr.* 16: 293, 1990.

PURPURA, K., VICTOR, J. D., AND KATZ, E. Striate cortex extracts higher-order spatial correlations from visual textures. *Proc. Natl. Acad. Sci. USA* 91: 8482–8486, 1994.

RATLIFF, F., KNIGHT, B. W., AND GRAHAM, N. On tuning and amplification by lateral inhibition. *Proc. Natl. Acad. Sci. USA* 62: 733–740, 1969.

RICHMOND, B.J., OPTICAN, L.M., PODELL, M., AND SPITZER, H. Temporal encoding of two-dimensional patterns by single units in primate inferior temporal cortex. I. Response characteristics. *J. Neurophysiol.* 57: 132–146, 1987.

SCHROEDER, C. E., TENKE, C. E., GIVRE, S. J., AREZZO, J. C., AND VAUGHAN, H. G., JR. Striate cortical contribution to the surface-recorded pattern-reversal VEP in the alert monkey. *Vision Res.* 31: 1143–1157, 1991.

SMITH, V. C. AND POKORNY, J. Spectral sensitivity of the foveal cone photopigments between 400 and 500 nm. *Vision Res.* 15: 161–171, 1975.

SUTTER, E. A practical nonstochastic approach to nonlinear time-domain analysis. In: *Advanced Methods of Physiological System Modelling*, edited by V. Marmarelis. Los Angeles, CA: Biomedical Simulations Resource, 1987, p. 303–315.

SUTTER, E. The fast m-transform: A fast computation of cross-correlations with binary m-sequences. *SIAM J. Comput.* 20: 686–694, 1991.

TOOTELL, R. B. H., SILVERMAN, M. S., HAMILTON, S. L., DE VALOIS, R. L., AND SWITKES, E. Functional anatomy of macaque striate cortex. III. Color. *J. Neurosci.* 8: 1569–1593, 1988.

VICTOR, J. D. Nonlinear systems analysis in vision: overview of kernel methods. In: *Nonlinear Vision: Determination of Neural Receptive Fields, Function, and Networks*, edited by R. Pinter and B. Nabet. Cleveland, OH: CRC, 1992, p. 1–37.

VICTOR, J. D. AND CONTE, M. M. Cortical interactions in texture processing: scale and dynamics. *Visual Neurosci.* 2: 297–313, 1989.

VICTOR, J. D. AND CONTE, M. M. Spatial organization of nonlinear interactions in form perception. *Vision Res.* 31: 1457–1488, 1991.

VICTOR, J. D. AND MAST, J. A new statistic for steady-state evoked potentials. *Electroencephalogr. Clin. Neurophysiol.* 78: 378–388, 1991.